LETTERS
https://doi.org/10.1038/s41567-021-01419-5

nature physics

Bulk and edge properties of twisted double bilayer graphene

Yimeng Wang[1], Jonah Herzog-Arbeitman[2], G. William Burg[1], Jihang Zhu[3], Kenji Watanabe[4], Takashi Taniguchi[5], Allan H. MacDonald[3], B. Andrei Bernevig[2] and Emanuel Tutuc[1]✉

The emergence of controlled, two-dimensional moiré materials[1–6] has uncovered a new platform for investigating topological physics[7–9]. Twisted double bilayer graphene has been predicted to host a topologically non-trivial gapped phase with Chern number equal to two at charge neutrality, when half the flat bands are filled[8,9]. However, it can be difficult to diagnose topological states using a single measurement because it is ideal to probe the bulk and edge properties at the same time. Here we report a combination of chemical potential measurements, transport measurements and theoretical calculations that show that twisted double bilayer graphene can host metallic edge transport in addition to simultaneously being insulating in the bulk. A Landauer–Büttiker analysis of the measurements on multi-terminal samples allows us to quantitatively assess the edge-state scattering. We interpret these results as signatures of the predicted topological phase at charge neutrality, but further characterization of the edge transport is required to be certain.

The tunability of moiré materials[1–6] by angle and carrier density powers the realization of novel topological phases[7–9], such as correlated Chern insulators that break time-reversal symmetry[10–16]. A long moiré period justifies low-energy effective models that neglect[17] weak scattering between the distant regions of momentum space known as valleys. The application of a transverse electric field causes bulk twisted double bilayer graphene (TDBG) to open a gap at charge neutrality to a topological state analogous to the quantum spin Hall state characterized by a non-zero valley Chern number $C_V = 2$ (refs. [8,9]), indicating two pairs of counter-propagating edge states per spin. However, the disruption of the moiré pattern on the edge is expected to break the valley symmetry, leaving the states susceptible to scattering and their fate uncertain.

A simultaneous investigation of the bulk and edge properties is necessary to reveal the band topology of an electronic system. We employ a sample design (Fig. 1a) that allows simultaneous electron transport and chemical potential measurements. Our samples consist of a double layer where one layer is a controlled moiré material (TDBG), with a twist angle (θ) ranging within 0.97−1.60°. The second layer is a graphene back gate (GrBG), consisting of monolayer or bilayer graphene with terminals for resistance measurements. The TDBG and GrBG layers are separated by a hexagonal boron nitride (hBN) dielectric. The GrBG acts not only as the back gate but also as a Kelvin probe for measuring the chemical potential of TDBG[18,19]. The double layer is encapsulated in hBN, with an added graphite top gate and placed on a SiO_2/Si substrate that serves as an additional gate. This sample architecture allows access to the chemical potential of the TDBG in a wide range of carrier densities (n) and transverse electric fields (E). Similar double layers have been used to probe chemical potentials and thermodynamic gaps in bilayer graphene[19], and twisted bilayer graphene[14], although without control of the transverse electric field. An optical micrograph of the sample is illustrated in Fig. 1b.

The longitudinal resistance (R_{xx}) of the TDBG is measured as a function of the top-gate bias (V_{TG}) and graphene back-gate bias (V_{BG}) to determine the twist angle, as well as to characterize the sample quality. The V_{TG} and V_{BG} values independently tune n and E according to the following relations: $n = (C_{TG}V_{TG} + C_{BG}V_{BG})/e$ and $E = (C_{TG}V_{TG} - C_{BG}V_{BG})/2\epsilon_0$, where e is the electron charge; ϵ_0 is the vacuum permittivity; and C_{TG} and C_{BG} are the capacitances per unit area of the top and back gate, respectively. The values of C_{TG} and C_{BG} can be first determined from the dielectric thickness, and confirmed with magnetotransport measurements (Supplementary Section A). Figure 1c shows the contour plot of R_{xx} as a function of n and E, which exhibits resistance maxima at densities commensurate with $n_s = 2.2 \times 10^{12}\,\mathrm{cm}^{-2}$ associated with filling of one moiré band with four-fold spin–valley degeneracy. The resistance maxima are observed at $n = 0, \pm n_s$ and $\pm 3n_s$, consistent with single-particle band structure calculations, as well as correlated insulators at $n = \pm n_s/2$ (refs. [3–6]). The R_{xx} maxima at $n = \pm 2n_s$ are a surprise because no gap between the second and third moiré bands is predicted in the single-particle band structure calculations. We tentatively attribute the R_{xx} maxima at $n = \pm 2n_s$ to a gap opening driven by electron–electron interactions. The twist angle (θ) can be extracted using the equation $n_s = \frac{8}{\sqrt{3}}\left(2a^{-1}\sin(\theta/2)\right)^2$, where $a = 2.46$ Å is the lattice constant of graphene. Figure 1d shows a line cut of R_{xx} versus n measured along the dashed line in Fig. 1c. Sharp R_{xx} peaks at integer $n/n_s = 0, \pm 1, -2$ and $+3$, as well as fractional $n/n_s = +1/2$, further illustrate the observations in Fig. 1c, highlighting the high quality of the TDBG sample.

We primarily focus on the TDBG properties at charge neutrality where one of the two flat bands per valley per spin is filled. The bulk topology[20] can be determined from the Bistritzer–MacDonald Hamiltonian[17]. Figure 1e shows how the twisting of the two graphene Brillouin zones forms the moiré Brillouin zone for the K valley. In Fig. 1f, we show the calculated band structure at an applied interlayer potential $V = 15$ meV using the parameters in ref. [20], and highlight the highest valence band at charge neutrality, labelled as −1. This band carries a Chern number of +2; because all the lower bands carry a zero Chern number, the total Chern number of the

[1]Microelectronics Research Center, Department of Electrical and Computer Engineering, The University of Texas at Austin, Austin, TX, USA. [2]Department of Physics, Princeton University, Princeton, NJ, USA. [3]Department of Physics, The University of Texas at Austin, Austin, TX, USA. [4]Research Center for Functional Materials, National Institute of Materials Science, Ibaraki, Japan. [5]International Center for Materials Nanoarchitectonics, National Institute of Materials Science, Ibaraki, Japan. ✉e-mail: etutuc@mail.utexas.edu

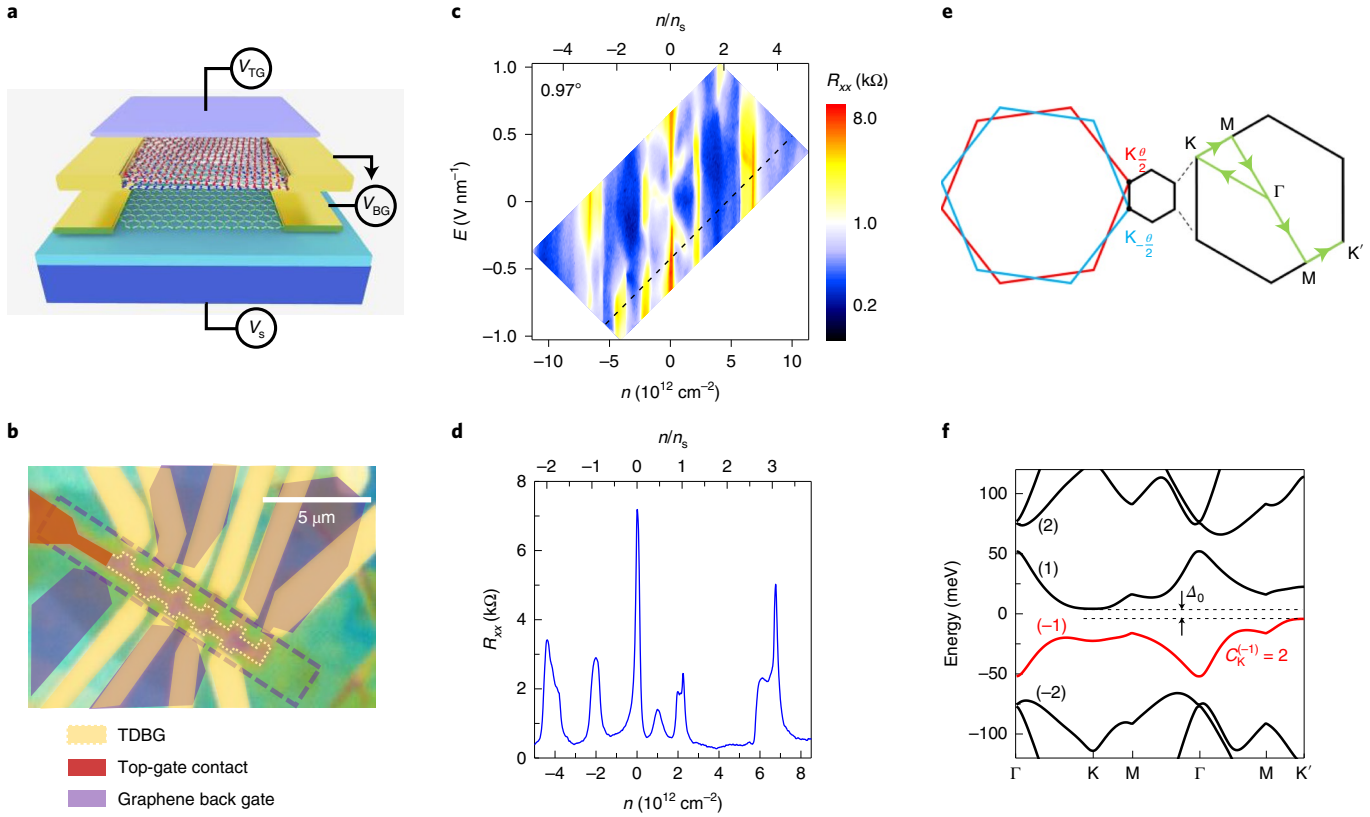

Fig. 1 | Sample layout, electrical transport and band structure. a, Schematic of the TDBG sample structure, with a graphite top gate and monolayer or bilayer graphene back gate. The substrate is separated from the dual-gated TDBG by a dielectric layer. The top gate, back gate and substrate are individually biased. **b**, Optical micrograph of a TDBG sample. The active area, top gate and back gate are marked. **c**, R_{xx} versus n and E, measured in a TDBG sample with $\theta = 0.97°$ at $T = 1.5$ K. **d**, R_{xx} versus n measured along the dashed line in **c**. The top axis shows the moiré band filling factor n/n_s in **c** and **d**. The data show R_{xx} maxima at integer and fractional filling factors. **e**, Schematic of the moiré Brillouin zone. $K_{\theta/2}$ and $K_{-\theta/2}$ are the two bilayers Brillouin zone corners. **f**, Calculated moiré band structure of TDBG in the K valley for $\theta = 1.60°$ and $V = 15$ meV, along the line-cut shown in **e**. The charge neutrality gap (Δ_0) is shown. The Chern number of the first valence band in the K valley is 2.

occupied bands is $C_K = 2$. The K′ valley is related to K by time reversal and must have an opposite Chern number. Therefore, the phase is characterized by the valley Chern number $C_V = (C_K - C_{K'})/2 = 2$ at charge neutrality.

By tuning the GrBG doping (n_{BG}) with a substrate bias (V_s), we are able to directly probe the TDBG chemical potential (μ) as a function of both n and E. An analysis of the band alignment in the heterostructure (Supplementary Section B) shows that when the GrBG is charge neutral ($n_{BG} = 0$), the TDBG chemical potential satisfies the following relation:

$$\mu = eV_{BG}\left(1 + \frac{C_s}{C_{BG}}\right) - eV_s\frac{C_s}{C_{BG}}, \quad (1)$$

where C_s is the capacitance per unit area between the substrate and GrBG. To determine the charge neutrality gap at different E fields, we utilize equation (1) and the data in Fig. 2a (Fig. 2a shows a contour plot of R_{xx} versus V_{TG} and V_{BG} for a TDBG sample with $\theta = 0.97°$). Along the black dashed diagonal, the TDBG carrier density is $n = 0$, whereas the E field varies. By mapping the longitudinal resistance of the GrBG (R_{BG}) versus V_{TG} and V_{BG} and tracking the charge neutrality of GrBG, μ can be extracted according to equation (1). Figure 2b–d shows three contour plots of R_{BG} versus V_{TG} and V_{BG} in the vicinity of $n_{BG} = 0$, measured at different V_s values. The corresponding V_{TG} and V_{BG} ranges used in Fig. 2b–d are marked by rectangles in Fig. 2a. By changing the V_s value at which the R_{BG} versus V_{TG} and V_{BG} data are acquired, the E-field value at the intersection point of the $n = 0$ and $n_{BG} = 0$ lines can be tuned accordingly. Indeed, the charge neutrality gaps of TDBG are measured at three E values, namely, 0.15 V nm^{-1} (Fig. 2b), 0.37 V nm^{-1} (Fig. 2c), and 0.29 V nm^{-1} (Fig. 2d). The black dashed lines in Fig. 2b–d illustrate the evolution of the charge neutrality of GrBG with V_{TG} and V_{BG}, which can be readily converted into a μ versus n dependence using equation (1). The clear step in the charge-neutrality line of GrBG observed as it crosses the $n = 0$ line of TDBG shown in Fig. 2c,d reveals a thermodynamic gap at the charge neutrality of TDBG. In contrast to the data in Fig. 2c,d, in Fig. 2b, the $n_{BG} = 0$ line is flat at $n = 0$, indicating the absence of a gap at a low E field. Due to our emphasis on the charge neutrality of TDBG in this work, we show R_{BG} versus V_{TG} and V_{BG} only in the vicinity of the double neutrality, that is, $n = n_{BG} = 0$, as shown in Fig. 2b,c. However, the μ values can also be probed away from $n = 0$. Indeed, Fig. 2d shows a contour plot of R_{BG} versus V_{TG} and V_{BG} that captures a wider density range for TDBG, and displays features that indicate gaps at other moiré filling factors.

Figure 2e summarizes the μ versus n dependence near $n = 0$ at varied E values. The μ versus n step at $n = 0$ marks the opening of a gap (Δ_0) that increases with the applied E field. The evolution of Δ_0 versus E for two samples with $\theta = 0.97°$ and $\theta = 1.60°$ is shown in Fig. 3a. For comparison, the data in Fig. 3a include the gap at charge neutrality measured in Bernal-stacked bilayer graphene as a function of the E field[19]. In both samples, the Δ_0 values exceed 100 K at large E fields, and are as high as 300 K in the $\theta = 0.97°$ TDBG.

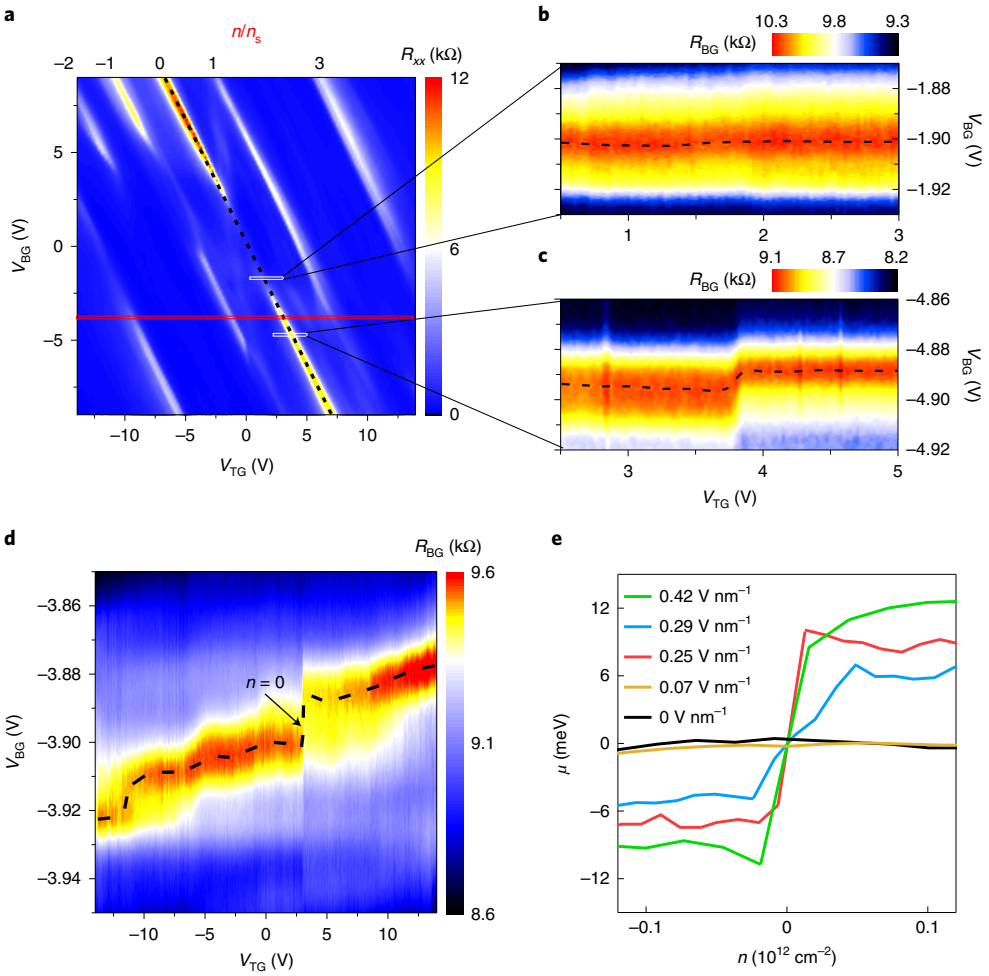

Fig. 2 | Chemical potential measurements. a, Contour plot of R_{xx} versus V_{TG} and V_{BG} measured in a TDBG sample with $\theta = 0.97°$. The moiré band filling factors corresponding to the R_{xx} maxima are labelled in red. The black dashed line marks the charge neutrality of TDBG. **b**–**d**, R_{BG} versus V_{TG} and V_{BG}. The black dashed lines mark the R_{BG} maxima indicating the charge neutrality loci of GrBG ($n_{BG} = 0$). The corresponding V_{TG} and V_{BG} ranges used in **b** and **c** are marked by the white rectangle and those in **d** are marked by the red rectangle in **a**. The data in **a**–**d** are measured at $T = 1.5$ K. **e**, μ versus n at different E-field values, in the vicinity of $n = 0$. Here Δ_0 can be extracted from the change in μ at $n = 0$.

Figure 3b shows the longitudinal resistivity (ρ_{xx}) versus E measured at $n = 0$ for three TDBG samples with θ values between 0.97° and 1.60°. The E-field range where Δ_0 opens in the $\theta = 0.97°$ sample is highlighted. The ρ_{xx} values remain low in the E-field range where Δ_0 is negligible, and show a sharp increase concomitant with the gap opening. Surprisingly, the ρ_{xx} values of TDBG then decrease with increasing E, and remain well within the expected range of a metallic electron system ($< h/e^2$, where h is the Planck's constant) despite the gap opening for all three samples. We note that similar low R_{xx} values at $n = 0$ and at high E fields can be seen in previous studies[21,22]. Figure 3b also shows ρ_{xx} versus E at $n = 0$ for a Bernal-stacked bilayer graphene[19]. Although both TDBG and Bernal-stacked bilayer graphene have a E-field-dependent gap at neutrality, the ρ_{xx} versus E dependence of the Bernal-stacked bilayer graphene is markedly different, quickly reaching large values with increasing E, as expected for a prototypical band insulator. Figure 3c shows the ratio of the non-local resistance (R_{NL}) to R_{xx} as a function of n and E measured in the 0.97° TDBG. The schematic of the measurement configuration for R_{NL} and R_{xx} is shown in Fig. 3c, inset. These data show a large R_{NL}/R_{xx} ratio at charge neutrality and at high E fields when Δ_0 opens, which signals a distinct change in the current pattern. It is noteworthy that both R_{NL} and R_{xx} values remain well below h/e^2 at charge neutrality, and the R_{NL}/R_{xx} ratio remains small elsewhere (Fig. 3c, contour plot). The sharp increase in the R_{NL}/R_{xx} ratio at charge neutrality combined with the low ρ_{xx} values when Δ_0 opens suggests the presence of edge transport when the TDBG is gapped.

The presence of edge transport may not necessarily stem from the non-trivial bulk topology. Indeed, electrostatic edge states due to a finite sample width can emerge in small-bandgap semiconductors[23]. To further test the origin of edge transport in TDBG, it is important to examine a similar twisted system, but with a topologically trivial gap. To this end, in Fig. 3b, we include ρ_{xx} versus E measured at $n = 0$ for a TDBG with $\theta = 181.10°$, that is, twisted at a small angle with respect to 180°. The additional data measured in a TDBG with $\theta = 181.9°$ can be found in Supplementary Section C. TDBGs with $\theta \approx 180°$ have a similar band structure as the TDBGs with $\theta \approx 0°$, and open a gap at $n = 0$ at finite E fields (Supplementary Section D). The magnetotransport properties of the 181.10° TDBG (Supplementary Fig. 2) reveal a rich Hofstadter butterfly comparable to samples with $\theta \approx 0°$ (Supplementary Fig. 1), indicating a similarly high-quality sample. However, owing to the C_{2y} symmetry in TDBGs with $\theta \approx 180°$, the gap at neutrality is topologically trivial with $C_V = 0$ (ref. [9]). Figure 3d compares ρ_{xx} versus E at $n = 0$ at different temperatures measured in the 181.10° TDBG (Fig. 3d, left) with ρ_{xx} versus E at $n = 0$ for the three TDBGs twisted with respect

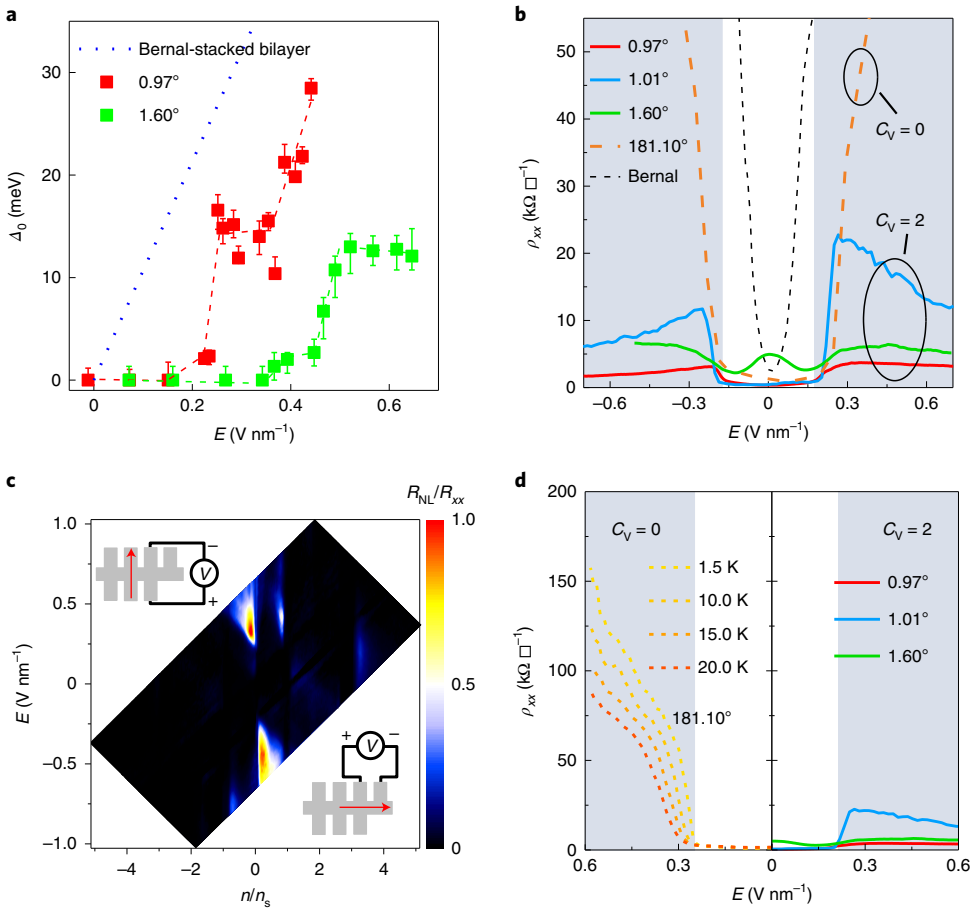

Fig. 3 | Gapped bulk and edge states. a, Charge neutrality thermodynamic gap Δ_0 versus E for two TDBG samples and Bernal-stacked bilayer graphene. The Δ_0 value in TDBG increases rapidly at a finite E, and remains finite once it is open. The red and green dashed lines are guides to the eye. The error bars represent the measurement uncertainty. **b**, ρ_{xx} versus E at charge neutrality measured in the $\theta = 0.97°$, 1.01°, 1.60° and 181.10° TDBG samples. The shaded areas mark the gapped region for the 0.97° TDBG. In the 0.97°, 1.01° and 1.60° samples, the ρ_{xx} values show an initial increase when the gap opens, but subsequently decrease with increasing E. In contrast, ρ_{xx} increases with E to values larger than h/e^2 in the 181.10° sample. The ρ_{xx} versus E measured at $n = 0$ in a Bernal-stacked bilayer graphene is included. **c**, Contour plot of R_{NL}/R_{xx} versus n/n_s and E measured in the 0.97° TDBG sample. The insets show the schematic of the measurement configuration for R_{NL} (upper left) and R_{xx} (lower right); the arrows mark the current direction. The large $R_{NL}/R_{xx} \approx 1$ ratio at $n/n_s = 0$ and finite E fields indicates edge transport. **d**, Left: temperature dependence of ρ_{xx} versus E at $n = 0$ measured in the 181.10° sample. The shaded area marks the gapped region. Right: ρ_{xx} versus E measured in small-twist-angle TDBGs. The shaded area marks the gapped region for the 0.97° sample. The data in panels **a**–**d** are measured at $T = 1.5$ K unless stated otherwise.

to 0° (Fig. 3d, right). The contrast between the two sets of samples is noteworthy—ρ_{xx} quickly reaches values much larger than h/e^2, with an insulating temperature dependence in the 181.10° TDBG, whereas the TDBGs with $\theta \approx 0°$ show ρ_{xx} lower than h/e^2 when the gap opens at neutrality. The contrast between the 180° TDBG and 0° TDBGs suggests non-trivial edge transport in the TDBGs with $\theta \approx 0°$, associated with the emergence of a topological valley Chern insulator.

To better describe the band structure and topology of the TDBG, we compute a single-particle phase diagram for TDBG[20] for $\theta = 0.8–1.8°$ and varying V, controlled by the applied E field. We extract the indirect gap at charge neutrality Δ_0 from the band structure (Fig. 1f) and compute the Chern numbers of the occupied bands. Figure 4a shows a contour plot of Δ_0 versus θ and V, which reveals a gap closing and reopening (blue dashed line) for all the angles at small V. Beyond the gap closing, corresponding to larger E fields, we find a gapped topological phase with $C_V = 2$. The results are consistent with the experimental data in our samples. Interestingly, the data in Fig. 4a predict a trivial insulator for $\theta > 1.1°$ with a gap of approximately 2 meV at $E = 0$, which may account for the decrease in ρ_{xx} at small E fields for the 1.60° TDBG (Fig. 3b), and also observed for TDBGs with $\theta = 1.55–1.90°$ (ref. [24]).

Figure 4b,c shows the phase diagrams at $n/n_s = \pm 1$, dominated by a gapless phase and a trivial insulator. However, at $\theta \approx 0.9°$ and small E fields, a gapped state with $C_V = +1$ (shaded area) appears for both $n/n_s = \pm 1$. In this state, at $n/n_s = +1$ in the K valley, the upper flat band has a Chern number of −1, which only partially cancels the Chern number of +2 carried by all the valence bands. Similarly, at $n/n_s = -1$, the dispersive bands below the flat bands carry a Chern number of +1, and the lower flat band carrying a Chern number of +1 is unoccupied. It is noteworthy that in addition to the large R_{NL}/R_{xx} observed at $n = 0$, the data in Fig. 3c show satellites of finite R_{NL}/R_{xx} at $n/n_s = 1$, a possible signature of the topological state at this filling factor. There is also an R_{NL}/R_{xx} peak at $n/n_s = -1$, but with a weaker non-local resistance, indicating some degree of particle–hole symmetry breaking. This finding is consistent with the shaded region shown in Fig. 4c, which is interrupted by a metallic phase near $\theta = 0.97°$.

To quantitatively probe the edge-state transport (Fig. 4d), we employ the Landauer–Büttiker formalism[25–27]. The 1.60° TDBG

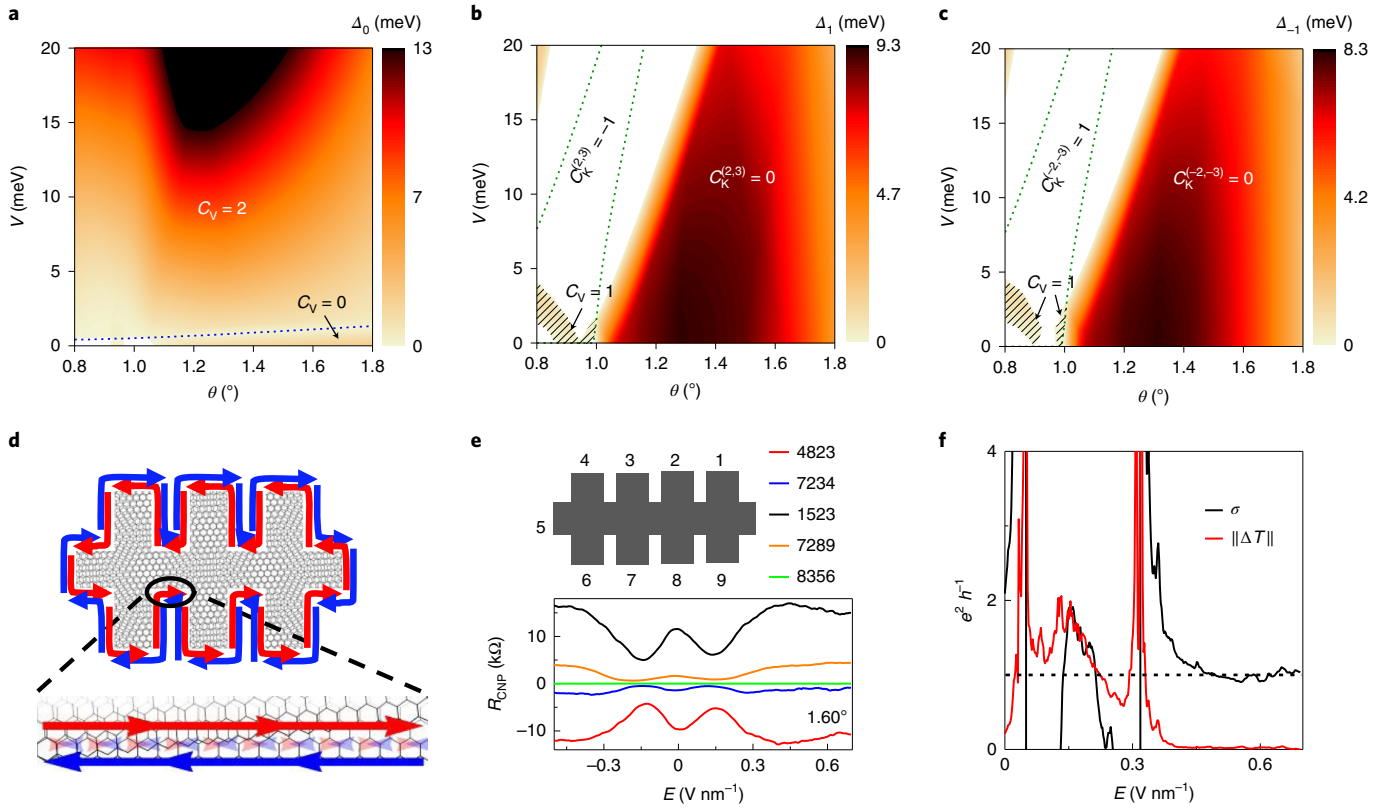

Fig. 4 | TDBG phase diagrams. a–c, The valley Chern number C_V as a function of θ and V for the gap between the lowest conduction band and highest valence band (Δ_0) (**a**), gap between the first and second conduction bands (Δ_1) (**b**) and gap between the first and second valence bands (Δ_{-1}) (**c**). The dashed lines indicate Chern number transitions in neighbouring bands, for example, $C_K^{(2,3)}$ ($C_K^{(-2,-3)}$) is the Chern number computed for the connected second and third conduction (valence) bands in the K valley. In **b** and **c**, the shaded areas mark the gapped regions with non-zero C_V at $n/n_s = +1$ and -1, respectively. **d**, Schematic of the counter-propagating edge states. Due to the breaking of valley symmetry, scattering on the edge can lead to localization. **e**, Examples of four-terminal resistance at charge neutrality (R_{CNP}) versus E measured in a multi-terminal TDBG with $\theta = 1.60°$. The four-digit notations (top) denote the measurement configurations in the form of (current in, current out, voltage+, voltage−). **f**, σ versus E calculated using 64 independent resistance measurements. $\sigma(E)$ diverges when the gap closes, and has values of the order of $e^2\,h^{-1}$ in the topological phase. For $E < 0.33\,\mathrm{V\,nm^{-1}}$, σ shows a large variation, expected in a bulk conductor. The norm of $\Delta T(E) = T(E) - T(0.7\,\mathrm{V\,nm^{-1}})$ is close to zero in the gapped phase, indicating that all $T(E)$ entries are insensitive to the applied E field.

has nine terminals, namely, $i = 1,\ldots,9$, which enables a variety of four-terminal resistance measurements relating the currents I_i and voltages V_i (Fig. 4e). The Landauer–Büttiker equation, normalized by $2C_V$ to include spin degeneracy, can be expressed as

$$I_i = 2C_V \frac{e^2}{h} \sum_{j=1}^{N} (T_{ji} V_i - T_{ij} V_j)\,. \tag{2}$$

Here T_{ij} is the transmission probability from $j \to i$ and $N = 9$ in our sample. Because of the disruption of the moiré pattern on the edge and the sample geometry, the transmission matrix T is not expected to take a simple form. We derive an exact inverse of the corresponding resistance measurements to the entries of T, extending previous results for a four-terminal sample[28] (Supplementary Section E). Using the matrix $T(E)$, we then extract the order parameter

$$\sigma(E) = \frac{2C_V e^2}{18h} \sum_{i \neq j}^{9} T_{ij}(E), \tag{3}$$

where the total edge conductance $\sigma = 4e^2/h$ when the edge states do not backscatter (Supplementary Section E.6). Figure 4f shows σ versus E and reveals a divergence in the order parameter at the topological phase transition at $E = 0.33\,\mathrm{V\,nm^{-1}}$. For larger E in the topological phase, σ quickly decays into a constant finite value. To further illustrate the edge transport, Fig. 4f shows $||\Delta T(E)||$, the average deviation of $T(E)$ from $T(0.7\,\mathrm{V\,nm^{-1}})$ defined by the Frobenius norm (Supplementary Section E.6). A small value of $||\Delta T(E)||$ means that $T(E)$ is close to $T(0.7\,\mathrm{V\,nm^{-1}})$ in every entry. Once the gap is open, we find that $||\Delta T(E)|| \approx 0$, indicating that the whole matrix $T(E)$ and the edge states described by it are independent of E, suggestive of topological effects.

Lastly, we comment on the contrast with Bernal-stacked bilayer graphene, a material with a large Berry curvature at the corners of the Brillouin zone and theoretically expected to possess edge states for specific terminations[29,30]. In TDBG, we find the transverse localization length of the edge state $\xi \approx 100\,\mathrm{nm}$, whereas $\xi \approx 1\,\mathrm{nm}$ in Bernal-stacked bilayer graphene (Supplementary Section F), making the edge states much more sensitive to edge disorder. This implies that the scattering of the edge states in TDBG is reduced owing to the long moiré period.

In summary, simultaneous thermodynamic and transport properties can provide unique insights into the effects of band topology in moiré materials, particularly for states that do not break time-reversal symmetry. The data suggest the possible emergence

of a tunable topological insulator in TDBG as a consequence of the non-zero valley Chern numbers of the moiré bands. However further characterization of the edge transport is required to establish the role of band topology.

Online content

Any methods, additional references, Nature Research reporting summaries, source data, extended data, supplementary information, acknowledgements, peer review information; details of author contributions and competing interests; and statements of data and code availability are available at https://doi.org/10.1038/s41567-021-01419-5.

Received: 14 September 2021; Accepted: 13 October 2021;
Published online: 20 December 2021

References

1. Cao, Y. et al. Correlated insulator behaviour at half-filling in magic-angle graphene superlattices. *Nature* **556**, 80–84 (2018).
2. Cao, Y. et al. Unconventional superconductivity in magic-angle graphene superlattices. *Nature* **556**, 43–50 (2018).
3. Burg, G. W. et al. Correlated insulating states in twisted double bilayer graphene. *Phys. Rev. Lett.* **123**, 197702 (2019).
4. Shen, C. et al. Correlated states in twisted double bilayer graphene. *Nat. Phys.* **16**, 520–525 (2020).
5. Cao, Y. et al. Tunable correlated states and spin-polarized phases in twisted bilayer–bilayer graphene. *Nature* **583**, 215–220 (2020).
6. Liu, X. et al. Tunable spin-polarized correlated states in twisted double bilayer graphene. *Nature* **583**, 221–225 (2020).
7. Wu, F., Lovorn, T., Tutuc, E., Martin, I. & MacDonald, A. H. Topological insulators in twisted transition metal dichalcogenide homobilayers. *Phys. Rev. Lett.* **122**, 086402 (2019).
8. Chebrolu, N. R., Chittari, B. L. & Jung, J. Flat bands in twisted double bilayer graphene. *Phys. Rev. B* **99**, 235417 (2019).
9. Koshino, M. Band structure and topological properties of twisted double bilayer graphene. *Phys. Rev. B* **99**, 235406 (2019).
10. Sharpe, A. L. et al. Emergent ferromagnetism near three-quarters filling in twisted bilayer graphene. *Science* **365**, 605–608 (2019).
11. Serlin, M. et al. Intrinsic quantized anomalous Hall effect in a moiré heterostructure. *Science* **367**, 900–903 (2020).
12. Wu, S., Zhang, Z., Watanabe, K., Taniguchi, T. & Andrei, E. Y. Chern insulators, van Hove singularities and topological flat bands in magic-angle twisted bilayer graphene. *Nat. Mater.* **20**, 488–494 (2021).
13. Das, I. et al. Symmetry-broken Chern insulators and Rashba-like Landau-level crossings in magic-angle bilayer graphene. *Nat. Phys.* **17**, 710–714 (2021).
14. Park, J. M., Cao, Y., Watanabe, K., Taniguchi, T. & Jarillo-Herrero, P. Flavour Hund's coupling, Chern gaps and charge diffusivity in moiré graphene. *Nature* **592**, 43–48 (2021).
15. Nuckolls, K. P. et al. Strongly correlated Chern insulators in magic-angle twisted bilayer graphene. *Nature* **588**, 610–615 (2020).
16. Choi, Y. et al. Correlation-driven topological phases in magic-angle twisted bilayer graphene. *Nature* **589**, 536–541 (2021).
17. Bistritzer, R. & MacDonald, A. H. Moiré bands in twisted double-layer graphene. *Proc. Natl Acad. Sci. USA* **108**, 12233–12237 (2011).
18. Kim, S. et al. Direct measurement of the Fermi energy in graphene using a double-layer heterostructure. *Phys. Rev. Lett.* **108**, 116404 (2012).
19. Lee, K. et al. Chemical potential and quantum Hall ferromagnetism in bilayer graphene. *Science* **345**, 58–61 (2014).
20. Burg, G. W. et al. Evidence of emergent symmetry and valley Chern number in twisted double-bilayer graphene. Preprint at https://arxiv.org/abs/2006.14000 (2020).
21. Sinha, S. et al. Bulk valley transport and Berry curvature spreading at the edge of flat bands. *Nat. Commun.* **11**, 5548 (2020).
22. He, M. et al. Symmetry breaking in twisted double bilayer graphene. *Nat. Phys.* **17**, 26–30 (2021).
23. Nichele, F. et al. Edge transport in the trivial phase of InAs/GaSb. *New J. Phys.* **18**, 083005 (2016).
24. Chu, Y. et al. Phonons and quantum criticality revealed by temperature linear resistivity in twisted double bilayer graphene. Preprint at https://arxiv.org/abs/2104.05406 (2021).
25. Büttiker, M. Four-terminal phase-coherent conductance. *Phys. Rev. Lett.* **57**, 1761–1764 (1986).
26. Büttiker, M. Absence of backscattering in the quantum Hall effect in multiprobe conductors. *Phys. Rev. B* **38**, 9375–9389 (1988).
27. König, M. et al. Quantum spin Hall insulator state in HgTe quantum wells. *Science* **318**, 766–770 (2007).
28. Büttiker, M. Symmetry of electrical conduction. *IBM J. Res. Dev.* **32**, 317–334 (1988).
29. Rozhkov, A. V., Sboychakov, A. O., Rakhmanov, A. L. & Nori, F. Electronic properties of graphene-based bilayer systems. *Phys. Rep.* **648**, 1–104 (2016).
30. Da Costa, D. R., Zarenia, M., Chaves, A., Farias, G. A. & Peeters, F. M. Energy levels of bilayer graphene quantum dots. *Phys. Rev. B* **92**, 115437 (2015).

Methods

Sample fabrication. All the graphene, graphite and hBN flakes used to fabricate our samples are mechanically exfoliated and inspected by optical microscopy. The hBN flakes are subsequently inspected with atomic force microscopy to confirm their thickness and surface roughness. Optical contrast and Raman spectroscopy are used to confirm the number of layers for monolayer and bilayer graphene. The TDBG samples are assembled by sequential pick-up steps utilizing a hemispherical polypropylene carbonate/polydimethylsiloxane handle. The back-gate structure is first prepared by picking up a monolayer or bilayer graphene with hBN, followed by a set of pre-trimmed graphite contacts. The stacked structure is then placed on a SiO_2/Si substrate, or a prepared hBN/graphite stack, in the case of samples with the graphite substrate gate, to form the bottom structure of the sample. Starting with another large bilayer graphene flake trimmed into two separate sections by lithography and O_2 plasma etching, another hBN is used to sequentially pick up the two sections—with the rotation of a small, controlled angle between the two pick ups—to form the TDBG. The TDBG is then placed on the bottom structure, and a graphite top gate is placed on the TDBG. The structure is then trimmed into a Hall-bar-shaped channel using CHF_3 and O_2 plasma etching, which also creates exposed one-dimensional edges of the TDBG and graphite contacts to the back gate. Metal (Cr/Pd/Au) edge contacts are evaporated to finalize the sample.

Measurement setup. The samples are measured in a variable-temperature liquid ^{4}He cryostat with a base temperature of 1.5 K. Three- and four-point resistance measurements with low-frequency (7–13 Hz) lock-in techniques are performed on the TDBG and GrBG layers. The source currents of different frequencies are used on the TDBG and GrBG layers to avoid crosstalk. A radio-frequency transformer is used to flow an a.c. current in the GrBG layer while applying a d.c. bias V_{BG}.

Data availability

Source data for Figs. 1–4 are provided with this paper. Data that support the findings of this study are available from the corresponding author upon reasonable request.

Code availability

A sample Mathematica code for performing the Landauer–Büttiker inversion is implemented for public use at https://doi.org/10.5281/zenodo.5539921. Any software package that can perform a singular-value decomposition is also suitable.

Acknowledgements

We thank Z.-D. Song and B. Lian for helpful discussions. The work at The University of Texas at Austin was supported by the National Science Foundation (NSF) grants MRSEC DMR-1720595, EECS-1610008 and EECS-2122476; Army Research Office under grant no. W911NF-17-1-0312; and the Welch Foundation grant F-2018-20190330. Work was partly done at the Texas Nanofabrication Facility supported by the NSF grant no. NNCI-2025227. B.A.B. was supported by the DOE grant no. DE-SC0016239, the Schmidt Fund for Innovative Research, Simons Investigator grant no. 404513, the Packard Foundation, the Gordon and Betty Moore Foundation through grant no. GBMF8685 towards the Princeton theory programme, and a Guggenheim Fellowship from the John Simon Guggenheim Memorial Foundation. Further support was provided by the NSF-EAGER no. DMR 1643312, NSFMRSEC no. DMR-1420541 and DMR-2011750, ONR no. N00014-20-1-2303, BSF Israel US foundation no. 2018226, and the Princeton Global Network Funds. J.H.-A. acknowledges support from a Marshall Scholarship funded by the Marshall Aid Commemoration Commission. A.H.M. acknowledges support from the Welch Foundation grant F1473. K.W. and T.T. acknowledge support from the Elemental Strategy Initiative conducted by the MEXT, Japan (grant no. JPMXP0112101001), and JSPS KAKENHI (grant nos. JP19H05790 and JP20H00354).

Author contributions

Y.W., G.W.B. and E.T. conceived the experiments. Y.W. and G.W.B. fabricated the samples and performed the experiments. J.H.-A., J.Z., A.H.M. and B.A.B. performed the theoretical calculations and analysis. K.W. and T.T. provided the hBN crystals. Y.W., J.H.-A, G.W.B., A.H.M. B.A.B. and E.T. analysed the data. Y.W., J.H.-A. and E.T. wrote the manuscript with input from all authors.

Competing interests

The authors declare no competing interests.

Additional information

Supplementary information The online version contains supplementary material available at https://doi.org/10.1038/s41567-021-01419-5.

Correspondence and requests for materials should be addressed to Emanuel Tutuc.

Peer review information *Nature Physics* thanks the anonymous reviewers for their contribution to the peer review of this work.

Reprints and permissions information is available at www.nature.com/reprints.